Available online at www.sciencedirect.com
ScienceDirect
Journal of Power Sources 161 (2006) 1084–1095
JOURNAL OF POWER SOURCES
www.elsevier.com/locate/jpowsour

On the mechanisms and behavior of coal syngas transport and reaction within the anode of a solid oxide fuel cell

R.S. Gemmen *, J. Trembly

National Energy Technology Laboratory, 3610 Collins Ferry Rd., Morgantown, WV 26507, United States

Received 13 March 2006; received in revised form 23 May 2006; accepted 6 June 2006
Available online 17 July 2006

Abstract

It is expected that in future years high temperature fuel cells will be coupled with coal gasification technology to produce electric power, as well as other valuable commercial products. Numerous technical investigations have already shown the feasibility of such systems at the system level as well as in the details of fuel cell operation. This paper focuses on the operation of an anode comprised of conventional solid oxide fuel cell anode materials (Ni/YSZ cermets) when operating on coal syngas. A model is presented for the transport of gases through the anode, as well as gas specie reactions within the anode consisting of methane reforming and water-gas shift. The model is validated by making comparisons to data and other models from the literature. The model is then employed to analyze transport performance within the anode over operating pressures between 1 and 15 atm. Results show the pressure effects on specie profiles, diffusion losses, and cell heating. Specifically, there is a maximum pressure (8 atm) under which hydrogen is produced by the methane-steam reaction; operating at higher pressure will produce methane. In addition, the concentration overpotential decreases as pressure increases from 1 to 5 atm after which it again increases. Finally, the model predicts a significant amount of heating due to the net reforming and water-gas shift reactions that should be considered by developers of these future systems.
Published by Elsevier B.V.

Keywords: Syngas; Coal; Solid oxide; Fuel cell; Anode; Model

1. Introduction

The U.S. Department of Energy is currently investing in the development of both fuel cell and coal gasification technologies [1]. Gasification technologies, along with new cleanup and sequestration technologies, allow for the environmentally benign use of coal for energy production, as well as the co-production of other beneficial products such as hydrogen, liquid fuels, etc. Given the vast quantities of coal resources within the U.S., it is logical to advance these technologies to support our future energy needs. To support this advancement, this paper specifically focuses on the coal syngas operation of SOFC anodes.

The financial cost of new technologies is always an issue. The use of a solid oxide fuel cell system can help to reduce plant costs, since the high efficiency of conversion results in a lower physical plant size for a given electric power output. As described by Kivisaari et al. [2], the necessary cleanup of the fuel gas for fuel cell operation can also be beneficial from a cost perspective, since it is easier to remove contaminates from the relatively low flow fuel stream than for conventional methods that use post-combustion cleanup which have much greater flow rates. For the above to become fully realized, however, low cost fuel cell technology must be achieved, and this will occur through the present DOE Solid State Energy Conversion Alliance (SECA) Program, Williams et al. [3]. Finally, low cost gas clean up methods that remove contaminates from coal syngas will also be needed, and this is also the subject of other DOE sponsored research.

1.1. Status and future plans of coal gasification for fuel cell derived power

Coal gasification is a process in which coal is transformed into a gaseous fuel containing a mixture of CO, H_2, CO_2, H_2O, CH_4, and N_2, as well as other minor species including some that

* Corresponding author. Tel.: +1 304 285 4536.
E-mail address: randall.gemmen@netl.doe.gov (R.S. Gemmen).

0378-7753/$ – see front matter. Published by Elsevier B.V.
doi:10.1016/j.jpowsour.2006.06.012

can shorten the life of the fuel cell. Coal is mixed with an oxidant (O_2) and steam in a reactor operating between 500 and 1800 °C and 25–70 atm (1 atm = 101.3 kPa) to produce the gaseous mixture known as syngas, Higman et al. [4] and Ratafia-Brown et al. [5]. Oxygen blown gasification is typically used since less combustion of coal is needed to heat the reactants to temperature and less work is needed to compress the gases entering the reactor Kivisaari et al. [2]. Further, given recent attention to CO_2 as a greenhouse gas, oxygen blown gasification will also help enable future sequestration technology. Three types of coal gasification systems have been used throughout industry; namely, moving bed, fluid bed, and entrained flow. Moving bed processes are characterized by large particles of coal that enter at the top of the reactor and the steam and oxygen enter at the bottom and operate at temperatures of 500–1250 °C and pressure of ≥30 atm [2,4,5]. Fluidized-bed reactors are characterized by high back mixing where ground coal (<6 mm) enters at the side of the reactor and the oxidant and steam enter near the bottom, which fluidizes the coal into the reacting bed. Fluidized-bed systems operate below the ash softening temperatures (950–1100 °C) and a pressure of approximately 25 atm [2,4]. The entrained flow reactor process is distinguished by its mixing of fine coal particles (<0.1 mm), dry or in the form of a water slurry, that enter at the top of the reactor with the oxidant and steam. Entrained flow gasification is also characterized by a very small residence time and high operating temperature range (1500–1700 °C) and pressures up to 70 atm. At present, entrained flow reactors have been the preferred choice for current IGCC systems and are anticipated to be used with future systems that also incorporate solid oxide fuel cell (SOFC) technology [2,4].

For entrained flow reactors, the product syngas composition is exceedingly dependent upon the gasification process, operating conditions, and the coal used in the process [2,4,6]. A summary of raw syngas compositions from the three major gasification systems is presented in Table 1. The oxygen and steam consumption by all three major processes is very similar [2].

Finally, it is noted that thus far very little SOFC operation has been performed directly on coal derived syngas. Recently, however, it has been reported that an SOFC using syngas from a circulating fluidized bed gasifier showed successful operation over a 75 h period, Shaffer [7]. These results are encouraging and offer a first look into the research needs for this future technology.

1.2. Paper objective and outline

While public literature provides several systems studies showing the performance of fuel cell systems when fuelled by coal syngas, e.g., Kivisaari et al. [2], no detailed investigations of coal syngas effects on fuel cell anode performance have been given. This paper investigates the detailed transport of coal derived syngas through the anode of an SOFC. A porous media model is derived, verified and validated with information from the literature, and then applied to syngas transport through an SOFC anode. The paper is organized as follows. Section 2 reviews past work related to this study. Section 3 describes the model developed for our work, and presents the literature data used for verification and validation of the model. Section 4 presents the results from the application of the model to syngas transport through the anode. Section 5 provides the summary and conclusions for this study.

2. Past work

Past literature provides support for the present study in the areas of mass transport in porous media, chemical reaction within porous catalyst media, fuel cell electrode performance and model prediction, and experimental data for validation.

2.1. Pure porous media transport (no chemical reactions)

Solcova et al. [8] compared two methods for the determination of the structural properties of porous media. The first via direct test methods (e.g., absorption and porosimetry methods) and the second via gas transport tests. They used both the mean transport pore model (MTPM) and the dusty gas model (DGM) in their determination of structural properties via the transport tests. They conclude that for simple mono-sized particles, the two methods compare fairly well, but for bi-dispersed particles the comparisons are not satisfactory. This indicates that the use of standard porosimetry methods to determine electrode structural properties used in model studies may not be generally viable. Instead, calibration of model parameters using direct experimental cell data will provide greater model utility. For the present work, we employ structural parameters representative of SOFC anodes as already published in the literature.

Table 1
Syngas gas compositions vs. gasifier types

	Gasifier type				
	Moving bed [2]	Fluidized bed [6]	Entrained flow [38]	Entrained flow (slurry fed) [6]	Entrained flow (dry fed) [6]
Gas composition (vol.%)					
CO	46.0	48.2	29.1	41.0	60.3
H_2	26.4	30.6	28.5	29.8	30.0
CO_2	2.9	8.2	11.8	10.2	1.6
H_2O	16.3	9.1	27.6	17.1	2.0
N_2	2.8	0.7	2.1	0.8	4.7
CH_4	4.2	2.8	0.009	0.3	0.0
HHV, Btu/dscf	333.0	309.0	213.7	278.0	297.0

Remick and Geankoplis [26] experimentally measured the diffusion of helium, neon and argon through a 39 μm dia. × 9.6 mm long capillary tube. By varying the operating pressure from 0.45 to 303 mmHg absolute, data spanning both Knudsen and molecular diffusion limits could be measured. This wide range of conditions and molecular weights allows the present work to validate the model developed to investigate coal syngas transport within an SOFC anode.

Kast and Hohenthanner [35] evaluate porous media transport from the continuum transport region to the free molecular transport region (i.e., Knudsen numbers below 0.01 and above 1.0, respectively). For the conditions of the present work where there is an interest in the pressurized operation of SOFC's for hybrid applications, the Knudsen numbers for all gas species is in the continuum where Knudsen diffusion is negligible, to near continuum region where Knudsen diffusion has a noticeable but relatively minor effect (see also the discussion below on Ackmann et al. [15]). From Kast and Hohenthanner, for these conditions the significance of pressure diffusion relative to ordinary diffusion is small, and can be estimated as, $n^{E}_{diff}/n^{ord}_{diff} = y\nabla p/p\nabla y = y\Delta p/p\Delta y$, where y is the mole fraction and p is pressure. As an example, for the mid-range in pressure for the present work (8 atm), we have approximately, $0.3 \times 800\,Pa/(808{,}000\,Pa \times 0.1) = 0.003$. Hence, it is not necessary to include effects of pressure diffusion for the present work.

2.2. CO and H_2 electro-kinetics and CH_4 reforming kinetics

Matsuzaki et al. [9] and Matsuzaki and Yasuda [10] studied the electrochemical characteristics of a $H_2 + H_2O + CO + CO_2$ system within a nickel and yittria-stablized-zirconia (YSZ) cermet electrode. The electrochemical oxidation rate of H_2 was found to be about two to three times greater than CO depending on operating temperature. They attributed this to the greater surface diffusion resistance of CO at low temperatures, and to both diffusion and charge transfer at high temperatures. In addition, the shift reaction was determined to be much faster than the electrode reactions over the temperature range studied.

Dicks [11] provided a review of kinetic studies on internal methane reforming in high temperature fuel cells. It is shown that considerable disagreement still exists for the reforming kinetics, especially in regard to the effect of steam partial pressure. In addition, as shown by Peters et al. [12], the effect of CO_2 causes a reduction in methane reformation, and more work is needed to provide reliable kinetic models.

Aguiar et al. [13] include the effects of methane steam reforming and water-gas shift in a one-dimensional model of an anode supported SOFC operated on a pre-reformed methane + steam mixture. The electrochemistry assumes only H_2 oxidation, and completely neglects any carbon-monoxide oxidation except through the water-gas shift reaction. Results show high methane reforming kinetics at the inlet to the anode, which quickly decays due to the consumption of methane. The work reported in the present paper on coal syngas focuses on the anode inlet behavior, and also shows high methane reforming kinetics of the residual methane present in the coal derived syngas, but only over a limited range of pressure.

It is evident from the above work investigating hydrogen and carbon monoxide oxidation kinetics that there is little consistency in the relative H_2-to-CO reactivity data. Some of the work suggests that carbon monoxide oxidation is at least a factor of one-third less than that of hydrogen, while in the modeling of fuel cell performance others ignore carbon monoxide oxidation altogether. For the present work, we will assume that some carbon monoxide is oxidized electrochemically. However, it is found that increasing the level of CO oxidation only changes the gas composition close to the electrolyte. That is, the gas composition throughout most of the electrode is unchanged due to changes in the relative consumption of H_2 and CO. This insensitivity is due to the fact that the water-gas shift reaction is fast, and equilibrates the H_2:CO mole fraction ratio regardless of which is consumed electrochemically.

2.3. Fuel cell electrode performance—electrochemistry and chemical kinetics

Achenbach and Riensche [14] studied the MSR and WGS reactions in a Ni–ZrO_2 cermet at conditions representative of natural gas fueled systems (partial pressure of CH_4 from 0.11 to 0.33 bar). They show that the high conversion rates of CH_4 at high temperatures (>850 °C) result in mass-transfer limiting conditions.

Ackmann et al. [15] investigated mass transport in SOFC cathodes and anodes using a MTPM. They show that for typical SOFC anodes operating on reformed methane syngas, neglecting Knudsen diffusion or permeation can result in up to 20% deviations. For the present paper, we include both Knudsen and permeation effects.

Bebelis et al. [16] also report on the kinetics of MSR on Ni/YSZ cermet electrodes. They show that over a range of methane and steam partial pressures the reforming kinetics can have variable order dependence on methane and steam content. They propose a competition between methane and steam dissociative adsorption on the nickel catalyst, and identified two rate limiting reaction steps (activated adsorption of methane and surface reaction of adsorbed carbon with adsorbed oxygen). The present authors view this type of work as developmental, and more work will be needed to understand MSR at this level of detail where surface kinetics can be included.

Lehnert et al. [17] modeled the effect of methane derived syngas on anode performance to determine the effect anode structural properties on methane conversion. The model considered molecular, Knudsen, and convective transport via a mean transport pore model (MTPM), and included effects for MSR and WGS. The kinetics for MSR and WGS were determined experimentally Drescher et al. [18]. Results showed that porosity and pore size control methane conversion most significantly (by 5–12%).

Recently, Haberman and Young [19] investigated the transport of methane derived syngas in the 1 mm thick porous support of a SOFC and also resolved conditions in the fuel stream-wise direction. Their model used the Darcy equation to describe convective transport due to pressure gradients, and the Stefan–Maxwell equation for bulk gas diffusion, and ignored

contributions from Knudsen diffusion due to an assumed large (10 μm) pore size. They used the same fuel supply composition and reforming kinetics used by Lehnert et al. [17]. No carbon-monoxide, only hydrogen electrochemical consumption was specified. Their results showed that for a case without reforming, little variation in specie concentrations exist through the highly porous support. Results also show an almost uniform hydrogen production rate (from reforming) in the direction of the thickness of the anode, which was higher at the inlet vs. exit by nearly two orders of magnitude. The hydrogen production followed the temperature profile, which was also nearly uniform through the thickness of the anode, high at the inlet, and significantly lower at the exit due to internal reforming.

Hecht et al. [20] provide a DGM for the transport of species through a porous Ni/YSZ cermet, and include a detailed kinetic model for MSR. They compare results of the model to experimental results from a hardware configuration that approximates the conditions of a true SOFC. The model incorporates 42 separate reaction mechanisms to account for MSR, WGS, and specie surface coverage. The comparison of model results to experimental results show overall good agreement in trends and specie concentrations. For a mixed CO_2/H_2O reforming case, worse case errors were for H_2 (27%), while for a pure H_2O reforming case, worse case errors were for CO (70%). Their results also highlight the fact that the reforming kinetics can be rate limiting for certain high load conditions. The present authors expect that the development of such detailed reaction kinetics for SOFC modeling will continue to evolve and improve as this technology matures.

3. Model description

3.1. Overview

Porous media, in general, exhibits two modes of mass transport. The first is pressure driven, which is commonly referred to as permeation transport. The second is diffusion transport which has two components—bulk molecular diffusion where molecular-to-molecular interaction dominates the transport, and Knudsen diffusion where molecular-to-solid wall interaction dominates the transport. All these transport mechanisms are believed to play a significant role within an SOFC anode. A representative configuration of an SOFC anode is shown in Fig. 1. As shown, the fuel gas is supplied via the anode gas channels. The various fuel components within the fuel gas then diffuse through the porous electrode to the electrolyte where they convert to their oxidized products. These products then counter-diffuse to the anode channel. Any non-reactive species that may be present within the anode gas (e.g., N_2) will, under steady conditions, exhibit zero net transport—exhibiting equal and opposite permeation transport and diffusion transport.

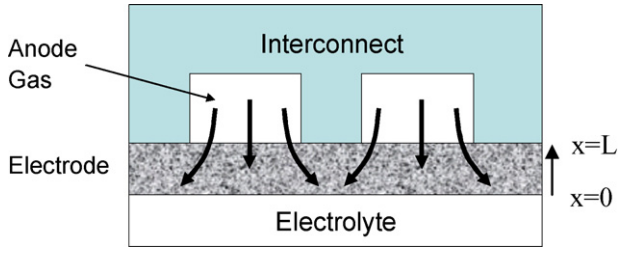

Fig. 1. Anode electrode having gas channels, interconnect, and electrolyte interfaces.

Permeation and Knudsen diffusion are affected by three porous media structural parameters: porosity, tortuosity, and pore size. Newer advanced SOFC anode electrodes are comprised of at least two layers having distinct structural properties: (1) an interlayer next to the electrolyte whose electrochemical performance is enhanced via particles with sizes ca. 20–50 nm providing increased active area; (2) a relatively thick (ca. 1 mm thickness) structural outer layer next to the interconnect having larger particle sizes (ca. 0.5–5 μm) providing increased gas transport. The objective of this work is to assess the transport and chemical kinetic concerns for coal syngas applications of SOFC's.

As shown in Section 1, several different approaches have been developed to evaluate multicomponent porous media transport problems having both permeation and diffusion transport mechanisms present. The mean transport pore model (MTPM) [8] and the dusty gas model (DGM) [21] both treat multicomponent diffusion transport using a modified Stefan–Maxwell model (SMM). For one-dimensional transport we have

$$-N_t \frac{dy_i}{dx} = \frac{n_i^d}{D_i^{*k}} + \sum_{j=1}^{J} \left(\frac{y_j n_i^d - y_i n_j^d}{D_{ij}^*} \right) \quad (1)$$

In the above equation x is the direction of flux, N_t (mol m^{-2} s^{-1}) is the total molar density, y (1) is the mole fraction, n^d (mol m^{-2} s^{-1}) is the mole flux due to molecular diffusion, D^{*k} (m^2 s^{-1}) is the effective Knudsen diffusion coefficient, D^* (m^2 s^{-1}) is the effective bimolecular diffusion coefficient, and J is the total number of gas species plus 1 (for the large dust particles). A subscript denotes the index value to a specific specie. The first term on the right of Eq. (1) accounts for Knudsen diffusion, and the following term accounts for multicomponent bulk molecular diffusion. As can be seen in Eq. (1), to account for Knudsen diffusion, the SMM is modified in a way that considers the two diffusion modes to operate in parallel. The MTPM and DGM are the same in their treatment of the molecular diffusion, but they differ in their treatment of permeation—MTPM employs the Weber permeation model and the DGM employs the Darcy permeation model. The former model includes a term accounting for viscous 'slip' at solid surfaces. For the present work on the evaluation of coal syngas transport through an SOFC anode, we employ the DGM.

3.2. Model equations

3.2.1. Dusty gas model

The DGM assumes that the porous media is comprised of spherical particles that behave as very large (and, hence, very slow moving) molecules. Because of the random assembly of these particles (which also have a distribution of sizes), the model assumes the use of effective diffusion transport coeffi-

cients for all molecular species

$$D_{ij}^{*} = D_{ij}\frac{\varepsilon}{\tau} \tag{2}$$

where, D_{ij} ($m^2\,s^{-1}$) is the bi-molecular diffusion coefficient, ε (1) is the bulk porosity, and τ (1) is the bulk tortuosity of the porous media. Diffusion coefficients were determined using the procedures outlined in Cussler [22]. Likewise, the effective Knudsen diffusion coefficient is defined as

$$D_i^{*\mathrm{k}} = D_i^{\mathrm{k}}\frac{\varepsilon}{\tau} = \left(\langle r\rangle\frac{2}{3}\sqrt{\frac{8RT}{\pi M_i}}\right)\frac{\varepsilon}{\tau} \tag{3}$$

where $\langle r\rangle$ (m) is the mean pore radii, R ($J\,mol^{-1}\,K^{-1}$) is the universal gas constant, and T (K) is the temperature. As mentioned above, the DGM uses the Darcy model for permeation. For one-dimensional transport we have

$$n_{\mathrm{t}}^{\mathrm{p}} = -B_0\frac{\mathrm{d}N_{\mathrm{t}}}{\mathrm{d}x} \tag{4}$$

where n_{t} ($mol\,m^{-2}\,s^{-1}$) is the total mole flux, B_0 ($m^2\,s^{-1}$) is the effective permeation coefficient, and N_{t} ($mol\,m^{-3}$) is the total molar density which can be related to pressure through the ideal gas law. The three transport parameters, ε, τ, and B, need to be determined experimentally via correlation with the model.

The total flux of specie 'i' is the sum of the diffusion and permeation fluxes

$$n_i = n_i^{\mathrm{d}} + y_i n_{\mathrm{t}}^{\mathrm{p}} \tag{5}$$

Using Eq. (1) (applied to the large dust particles) and Eq. (4), along with the fact that the large 'dust particles' making up the porous media are immobile, the solution for $\mathrm{d}N_{\mathrm{t}}/\mathrm{d}x$ can be found in terms of the mole fluxes of the gas components. This solution can be substituted back into Eq. (5) for $\mathrm{d}N_{\mathrm{t}}/\mathrm{d}x$ to have, per Warren [23]

$$-N_{\mathrm{t}}\frac{\mathrm{d}y_i}{\mathrm{d}x} = \frac{n_i}{D_i^{*\mathrm{k}}} + \sum_{j=1}^{J}\left(\frac{y_j n_i - y_i n_j}{D_{ij}^{*}}\right) - \frac{B_0 y_i}{D_i^{*\mathrm{k}}}\left[\frac{\sum_{m=1}^{J}\left(\frac{n_m}{D_m^{*\mathrm{k}}}\right)}{1 + B_0\sum_{m=1}^{J}\frac{y_m}{D_m^{*\mathrm{k}}}}\right] \tag{6}$$

The above equation, for $i = 1$ to $J-1$, provides a linear set of independent ordinary differential equations. To solve for all J components, an additional equation is needed. For this we use the conservation of species

$$n^{\mathrm{T}} = \sum_{j=1}^{J} n_i \tag{7}$$

Eqs. (6) and (7) can be used to solve for the spatial distribution of mole fluxes and mole fractions for all J components.

For the solution, we note that Eq. (6) can be recast into matrix notation as

$$\bar{\bar{H}}\cdot\bar{n} + \overline{N_{\mathrm{g}}} = 0 \tag{8a}$$

where $\bar{n} = \{n_1, n_2, n_3, \ldots, n_J\}^{\mathrm{T}}$ is the vector of gas phase mole fluxes (molecular + permeation transport). The components for the submatrix $J-1\times J$ of $\bar{\bar{H}}$ are given by

$$H_{ii} = \frac{1}{D_i^{\mathrm{k}}} + \frac{y_i B_i}{D_i^{\mathrm{k}}} + \sum_{m=1}^{J}\left(\frac{y_m}{D_{im}}\right);\quad (m\neq i),$$

$$H_{ij} = \frac{y_i B_i}{D_j^{\mathrm{k}}} - \frac{y_i}{D_{im}};\quad (i\neq j),$$

$$B_i = -\frac{B_0/D_i^{\mathrm{k}}}{\left(1 + B_0\sum_{m=1}^{J}\frac{y_m}{D_m^{\mathrm{k}}}\right)},$$

$$B_0 = r^2\frac{\varepsilon}{\tau}\frac{p}{8\mu}\quad (1\le i\le J-1) \tag{8b}$$

where p (Pa) is the pressure and μ ($Pa\,s^{-1}$) is the mixture dynamic viscosity. The above submatrix to $\bar{\bar{H}}$ provides an independent set of transport equations derived from Eq. (6). To provide the final Jth independent equation, the last row of $\bar{\bar{H}}$ is given by

$$H_{Jj} = 1 \tag{9}$$

Finally, the vector $\bar{N}_{\mathrm{g}}$ is given by

$$\bar{N}_g = \{\mathrm{d}N_1/\mathrm{d}x, \mathrm{d}N_2/\mathrm{d}x, \mathrm{d}N_3/\mathrm{d}x, \ldots, \mathrm{d}N_{J-1}/\mathrm{d}x, -n^{\mathrm{T}}\}^{\mathrm{T}} \tag{10}$$

which is the vector of gas phase mole density gradients, but with the last element being the negative of the total mole flux.

3.2.2. Conservation equation

Using Eq. (8b) with elements to H as defined in Eqs. (8b)–(10), solutions for the fluxes of n_i can be found in terms of the known distributions of specie concentrations. The calculated fluxes can then be used to determine the rate of change of specie concentrations through the following one-dimensional conservation equation

$$\varepsilon\frac{\mathrm{d}N_i}{\mathrm{d}t} = -\frac{\mathrm{d}n_i}{\mathrm{d}x} + R_i \tag{11}$$

where R_i ($mol\,m^{-3}\,s^{-1}$) is the rate of production of specie 'i' due to chemical reactions.

3.2.3. Chemical reactions

The principle reactions of concern for the present work are methane steam reforming (MSR) and water-gas shift (WGS). Following Lehnert et al. [17], these chemical reactions are accounted for, respectively, as

$$\mathrm{CH_4 + H_2O \underset{k_r^-}{\overset{k_r^+}{\longleftrightarrow}} 3H_2 + CO},\quad \Delta H_{298} = 206\,\mathrm{kJ\,mol^{-1}} \tag{12}$$

$$\mathrm{CO + H_2O \underset{k_a^-}{\overset{k_a^+}{\longleftrightarrow}} CO_2 + H_2},\quad \Delta H_{298} = -41\,\mathrm{kJ\,mol^{-1}} \tag{13}$$

The net forward reaction rate for MSR, Eq. (12), has previously been determined experimentally for a representative SOFC

anode by Divisek et al. [24] as reported in Lehnert et al. [17]. The net reaction rate is given as

$$R_r = k_r^+ p_{CH_4} p_{H_2O} - k_r^- p_{CO}(p_{H_2})^3 \quad (14)$$

where k_r^+ (mol m^{-3} s^{-1} Pa^{-2}) and k_r^- (mol m^{-3} s^{-1} Pa^{-4}) represent the forward and reverse rate constants, respectively. The water-gas shift reaction, Eq. (13), is considered to be very quick and remains in equilibrium throughout the SOFC anode. Per Lehnert et al., equilibrium of the WGS is represented by a kinetic expression with very high forward and reverse reaction rates

$$R_s = k_E^+ p_{CO} p_{H_2O} - k_s^- p_{CO_2} p_{H_2} \quad (15)$$

where k_s^+ (mol m^{-3} s^{-1} Pa^{-2}) and k_s^- (mol m^{-3} s^{-1} Pa^{-2}) represent the forward and reverse rate constants, respectively. The MSR and WGS rate constants reported by Lehnert et al. were analyzed by Haberman and Young [19] and reported in Arrhenius form (see Eqs. (16)–(22)). Because the results from Lehnert et al. were also used in this present work for model verification, adjustments were made so that accurate predictions were achieved for their 1123 K case. The resultant kinetic data used in the present work is given by

$$K_{ps} = \frac{k_s^+}{k_s^-} = \frac{p_{H_2} p_{CO_2}}{p_{H_2O} p_{CO}} \quad (16)$$

$$K_{pr} = k_r^+ / k_E^- = \frac{p_{CO}(p_{H_2})^3}{p_{CH_4} p_{H_2O}} \quad (17)$$

$$K_{ps} = (1.049)\exp(-0.2935Z^3 + 0.6351Z^2 + 4.1788Z + 0.3169) \quad (18)$$

$$K_{pr} = (1.003)(1.0267 \times 10^{10}) \times \exp(-0.2531Z^4 + 0.3665Z^3 + 0.5810Z^2 - 27.134Z + 3.2770) \quad (19)$$

$$Z = \frac{1000}{T(K)} - 1 \quad (20)$$

$$k_s^+ = (1.185)(0.0171)\exp\left(\frac{-103191}{RT}\right) \quad (21)$$

$$k_r^+ = (1.942)(2395)\exp\left(\frac{-231266}{RT}\right) \quad (22)$$

where K_{ps} [1] and K_{pr} (Pa^2) are the equilibrium constants for the WGS and MSR reactions, respectively.

Finally, the molar rates of formation for the various species in the system are presented in Eq. (23) through (27)

$$R_{CH_4} = -R_r \quad (23)$$

$$R_{CO} = R_r - R_s \quad (24)$$

$$R_{H_2O} = -R_r - R_s \quad (25)$$

$$R_{H_2} = 3R_r + R_s \quad (26)$$

$$R_{CO_2} = R_s \quad (27)$$

3.3. Numerical solution method

The DGM shown in Eq. (6) and the conservation equation shown in Eq. (11) are used to solve for the transient specie behavior within an anode electrode given prescribed boundary conditions. As explained in the following paragraphs, a custom software package was developed to provide the solution to the transient electrode diffusion problem.

3.3.1. Numerical model

A finite control volume analysis is employed for the numeric solution of Eq. (11). To avoid oscillations in the numerical solution, the locations for node properties (e.g., specie concentration, temperature and pressure) are offset by $1/2\Delta x$ from the flux node locations following Patankar [25]. The gradient term in Eq. (8) is given by central differencing, except at the end nodes where forward or backward differencing is required. The specified boundary conditions are specie concentration values at $x = L$ (see Fig. 1), and reactant consumption at $x = 0$. Reactant consumption at the electrolyte, R_e (as a mole flux of H_2 and CO into the electrolyte, and H_2O and CO_2 away from the electrolyte) is related to current through Faraday's law as follows:

$$R_{e\,H_2} = \frac{-i_{H_2}}{2F} = -R_{e\,H_2O} = \frac{i_{H_2O}}{2F} \quad (28)$$

$$R_{e\,CO} = \frac{-i_{CO}}{2F} = -R_{e\,CO_2} = \frac{i_{CO_2}}{2F} \quad (29)$$

where F is the Faraday constant (C mol^{-1}), and i_{H_2} (A m^{-2}) and i_{CO} (A m^{-2}) are the currents due to the electrochemical consumption of hydrogen and carbon-monoxide, respectively. Here it is assumed that a positive value for i_{H_2} indicates electrochemical consumption of H_2 (likewise for CO). The total current measured by instrumentation applied to a cell is the sum of the two currents, i_{H_2} and i_{CO}. As mentioned previously, there is no consistency in the literature regarding the treatment of combined CO and H_2 electrochemistry. Matsuzaki and Yasuda [10] suggest that the ratio of H_2:CO electrochemistry is 2:1, while Aguiar et al. [13] choose to ignore CO electrochemistry completely. For the work reported here on coal syngas oxidation, we assume that $i_{H_2} = 4i_{CO}$. The impact of changes in the relative consumption of H_2 and CO were examined, and shown to be limited mainly to the first 0.2 mm layer near the electrolyte due to the fast WGS reaction which equilibrates the H_2 and CO mole fractions.

3.3.2. Solution method

Initial conditions are given for all parameters at $t = 0$. To integrate in time, at time t an L-U decomposition matrix solver is used to solve for specie fluxes, $\bar{n}$, in Eq. (8) given known distributions of specie concentrations, $\bar{N}$. The specie concentrations at $t + dt$ are then calculated via Eq. (11) by explicit time integration.

In this paper, for both the model validation and application to SOFC electrodes, we focus only on the steady diffusion of reactants. Hence, the model was run until the solution was convergent and changes in reactant partial pressures through the electrode changed by less than one part in a thousand per second. For the

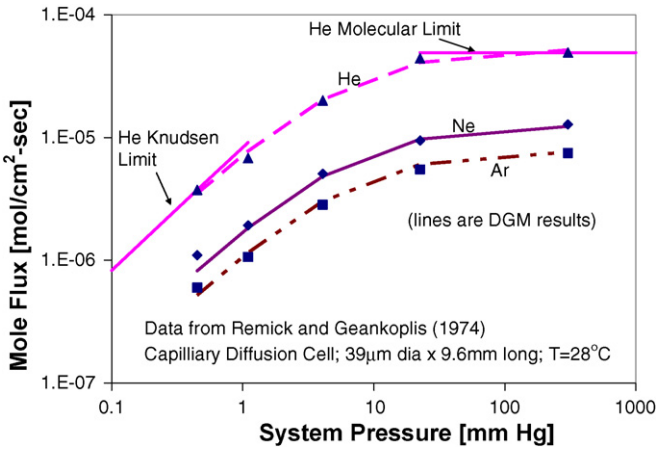

Fig. 2. DGM results (lines) compared to He + Ne + Ar capillary diffusion data of Remick and Geankoplis [26]. Results confirm that the DGM developed for diffusion studies accurately predicts both Knudsen and molecular limits of diffusion behavior.

SOFC electrode results presented below, 40 nodes were used to give sufficient node independent results. The computational time to reach steady state was about 30 min on a 1.7 GHz computer.

3.4. Model validation

The model was validated using data from the literature. To assess the accuracy of the model for pure diffusion spanning both Knudsen and molecular domains, data on the diffusion of helium, neon and argon through a 39 μm dia. × 9.6 mm long capillary tube was used, Remick and Geankoplis [26]. Here the pressure was varied over about three orders of magnitude in order to span the Knudsen and molecular diffusion limits for this ternary diffusion problem. Because the pressure and temperature were the same throughout the system, Graham's law applies, Mason and Malinkauskas [21]

$$\sum_i n_i \sqrt{\mathrm{MW}_i} = 0 \tag{30}$$

where MW_i (g mol^{-1}) is the molecular weight of specie 'i'. A total of 41 nodes were used through length of the capillary tube, and the model was run until steady state conditions were reached. Results for the model comparison with the experimental data are shown in Fig. 2. As can be seen, the model closely follows the experimental data. (As reported by Remick and Geankoplis [26], the average error in the diffusion fluxes from their theoretical value was about 5%.) In addition, the model curves follow both limits of Knudsen and molecular diffusion very closely. A test of node-number dependency on predicted results showed that beyond 20 nodes results were node independent. The results from this part of the validation work confirm that the DGM accurately predicts molecular diffusion in porous media.

Comparisons were also made with data from Yakabe et al. [27]. Here, the concentration overpotential through a 2 mm thick SOFC anode was measured for two different anode gas mixtures ($H_2 + H_2O + Ar$ and $CO + CO_2$) under different current loadings. Suwanwarangkul et al. [28] also used the Yakabe et al. [27] data in the comparison of Fickian, Stefan–Maxwell, and DGM models and found that the DGM provided best agreement with the data. We repeat their study as a way to validate the present model. It is pointed out, however, that the model developed by Suwanwarangkul et al. [28] assumed that Graham's law (Eq. (30)) applied because of negligible pressure gradient through the anode. However, applying Graham's law here forces improper flux relations between the species based on their ratio of molecular weights, rather than the physically correct Faradaic relations (Eqs. (28) and (29)). Also, while Suwanwarangkul et al. [28] found best model comparisons using a tortuosity of 4.5, our work found that improved comparisons to the data could be obtained with 5% less tortuosity. Results for the comparison using 41 nodes (and all other physical model parameters as shown in Suwanwarangkul et al. [28]) are shown in Fig. 3. As can be seen, the model developed here (denoted NETL DGM) shows a slightly improved comparison to the data. For both models, the comparison is poor at high current density and high overpotential (Fig. 3c and f). A sensitivity analysis shows, however, that at these conditions concentration overpotentials are sensitive to small changes in concentrations, and, hence, may not be as reliable for model comparison purposes. For example, small gas leakage may cause a high-bias in measured overpotentials, such as might be evident in Figs. 3c and f. Also, the models presented here and in Suwanwarangkul et al. do not account for surface diffusion transport that may exist near the electrolyte interface which contributes to the concentration overpotential, Williford et al. [29].

Finally, to verify the capability of the model to predict combined diffusion and reactive chemistry, comparisons were made with the model predictions given by Lehnert et al. [17] Here, a 2 mm thick porous SOFC anode running on 30% pre-reformed natural gas was simulated using a MTPM. The case used for model verification was: 1123 K, 300 mA cm^{-2}, $\varepsilon/\tau = 0.156$, $\langle r \rangle = 1.07\mathrm{e}{-6}$ m, $i_{H_2} : i_{CO} = 1$ (because of the fast WGS, model results away from the electrolyte boundary are largely insensitive to $i_{H_2} : i_{CO}$ ratio). Again, 41 nodes were used for the DGM, and the model was run until steady state conditions existed. Results for the DGM comparison with the results from Lehnert et al. [17] are shown in Fig. 4. As can be seen, very close comparisons exist for the CH_4 concentration profile and consumption profile. The consumption profiles for H_2O and CO are also closely followed. The greatest differences are in the total pressure, P_{total}, and H_2 profiles, which likely arise from the different permeation models.

4. Model application and results

As shown in Section 2, numerous investigators have studied the transport of reformed natural gas inside the anode of a solid oxide fuel cell. Here we specifically focus on the transport of coal syngas inside the anode, and in particular, examine the behavior at the inlet edge of the anode. Coal syngas compositions are much different from natural gas compositions, which will result in different behavior from that reported by others, Lehnert et al. [17]. The inlet edge of the anode is of particular interest given that any chemical non-equilibrium of the anode gas will

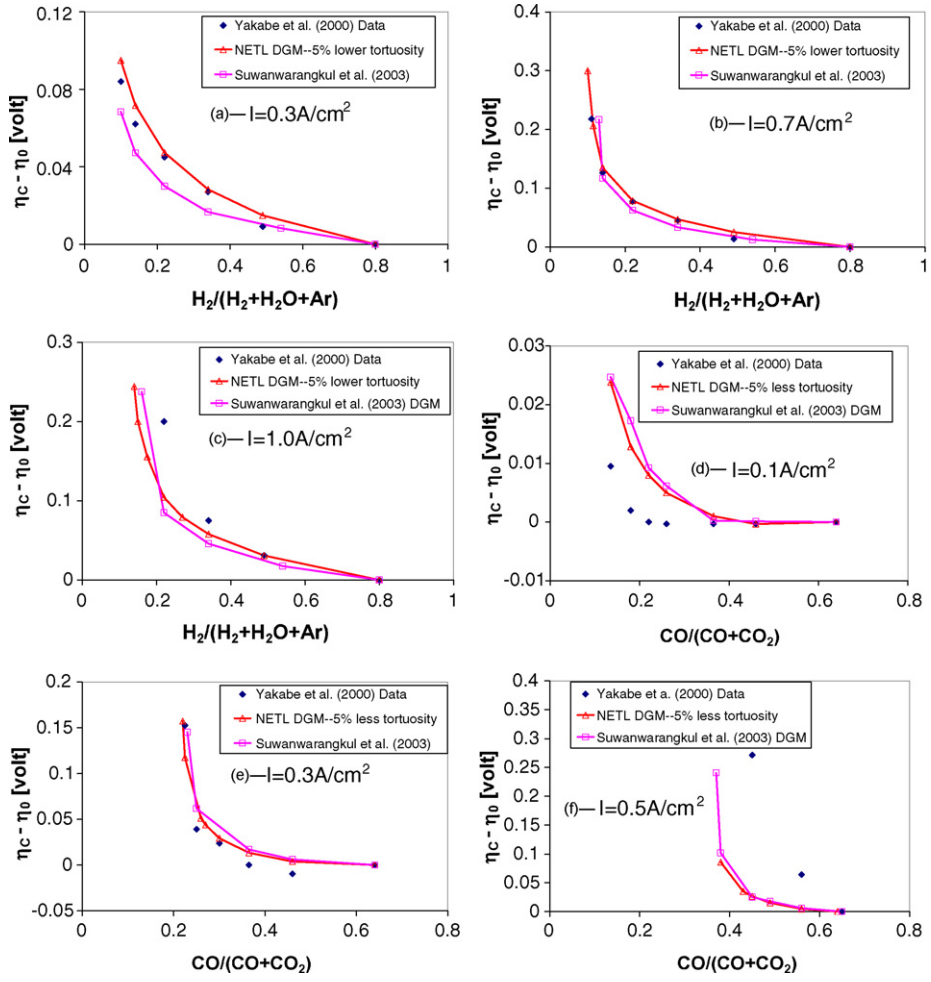

Fig. 3. NETL DGM compared to Suwanwarangkul et al. [28] DGM and Yakabe et al. [27] data. Best fit to the data for the NETL DGM occurred with a 5% lower tortuosity. For reasons suggested in the text, results show an overall slight improved comparison to the Yakabe et al. data and Suwanwarankul et al. model when using the NETL DGM.

cause significant heating/cooling as the nickel anode material catalytically converts the gases via the MSR and WGS reactions, Eqs. (12) and (13), respectively. The endothermic MSR reaction cools the anode, while the exothermic WGS reaction heats the anode. The extent of heating/cooling depends on the extent of non-equilibrium of the components, and to what side of the equilibrium point they exist (i.e., whether forward or backward reactions occur).

As shown in Section 1, compositions of coal syngas are varied, but overall contain more carbon, more oxygen, and less hydrogen than natural gas fueled systems, Yi et al. [30]. For the present work, the anode gas was assumed to have the syngas composition from Hoffman [31] shown in Table 1. Future work will examine the effects of other coal syngas compositions. As can be readily shown by minimization of the Gibbs free-energy, this syngas composition is in non-equilibrium for the tempera-

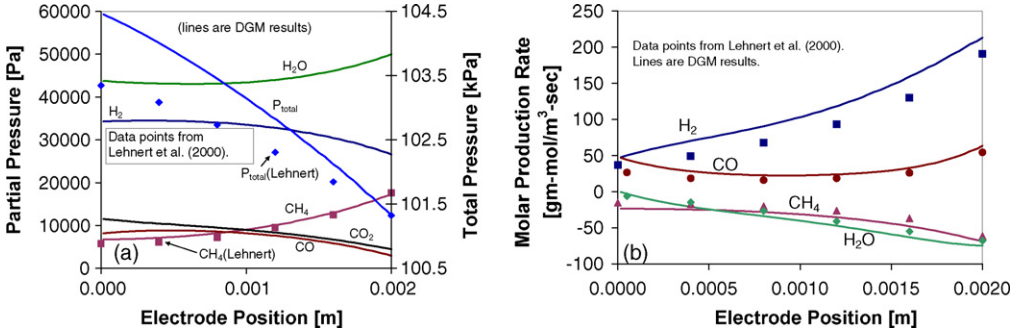

Fig. 4. DGM results (lines) compared to model results of Lehnert et al. [17]. (a) Concentration profiles; (b) molar production rates. Results show that overall close agreement exists between current work and that of Lehnert et al.

Table 2
Anode electrode properties

Parameter	Value
Thickness, L (m)	0.002
Tortuosity, τ	3.6
Permittivity, $\Psi = \varepsilon/\tau$	0.156
Mean pore diameter, $\langle r \rangle$ (μm)	1.07
Operating temperature, T (°C)	800

tures and pressures considered in this work, and would slightly (∼6 °C) cool due to the MSR and WGS reactions if allowed to equilibrate. However, gas phase kinetic calculations were performed showing that the composition does not significantly change from that shown in Table 1, even over time durations much greater than expected for transport from the gasification cleanup device to the fuel cell (<100 s), and even when at representative anode inlet conditions (e.g., ∼700 °C.) Hence, it is reliable to make the assumption that the syngas will reach the anode largely unaltered from the conditions exiting the gasifier (e.g., compositions reported in Table 1.)

The model is applied to an anode having properties as shown in Table 2. Because the optimal operating pressure of future coal based fuel cell systems is currently being evaluated, pressure was parametrically varied from 1 to 15 atm, while the temperature was fixed at 800 °C. This pressure range spans the pressures used in past system studies examining the application of solid oxide fuel cells to gasification based systems, Kivisaari [2].

4.1. Assessment of carbon deposition

To determine if carbon deposition may occur for these mixture and pressure conditions, thermodynamic equilibrium analysis was performed using the FACTSAGE software program developed by Thermfact Ltd. and GTT-Technologies mbH. For Ni/YSZ anodes, it is known that such calculations slightly overpredict the true deposition conditions, but at least provide a minimum steam-to-carbon requirement to avoid deposition, Clarke [32]. Results are presented in Fig. 5 showing that carbon deposition is close to being thermodynamically possible at the higher pressures considered for this work, but are still outside the deposition region. Further, it is well known, Weber et al. [33] and Gunji et al. [34], that the addition of oxygen to the anode via

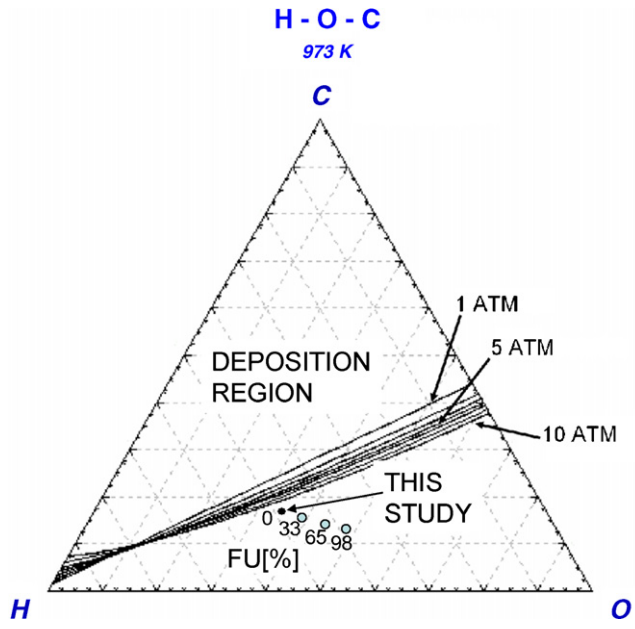

Fig. 5. Ternary diagram for carbon deposition equilibrium calculations. Data points indicate operating points for given fuel utilization (FU). Each corner shows the element having the 100% mole fraction value.

electrochemical conversion of fuel reduces the potential for carbon deposition. This reduction in carbon deposition potential is also shown in Fig. 5 as a percent of fuel utilization. A total of 41 nodes are used in the model, and the model was run until it reached steady state for all results presented.

4.2. Pressure effects

Results for a 300 mA cm^{-2} load are shown in Figs. 6–10. Fig. 6a shows the profile for hydrogen through the electrode. At 1 atm pressure operation, there is a mild increase in hydrogen content near the free-stream side of the electrode ($x = 0.002$ m) due to MSR and WGS. The hydrogen concentration then decreases toward the electrolyte ($x = 0.000$ m) due to electrochemical consumption of hydrogen. As pressure increases, there is an increase in hydrogen generation until about 7 atm, which lifts the entire concentration profile. At pressures higher than 7 atm, the mole fraction of hydrogen decreases. This decrease results directly from an overall decrease in hydrogen generation

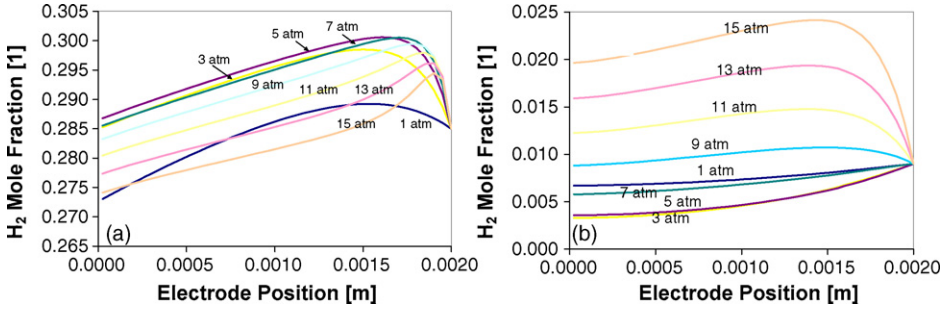

Fig. 6. Hydrogen and methane profiles through the electrode, (a) and (b), respectively, at 300 mA cm^{-2}. Because of both reforming and water-gas shift, there is a rise in hydrogen concentration at the free-stream side of the electrode. At about 8 atm and above, there is a net gain in methane concentration relative to free-stream conditions.

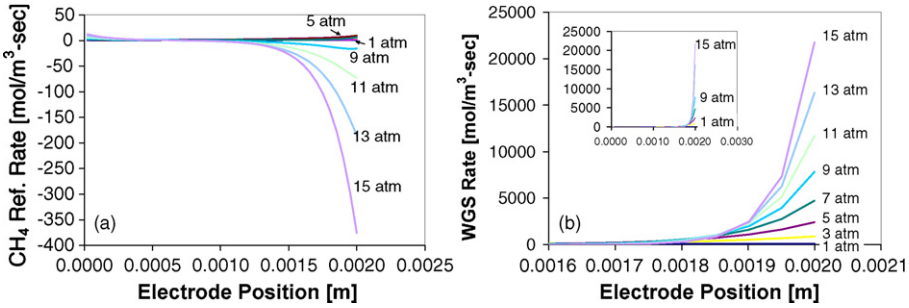

Fig. 7. MSR net forward reaction rate (a), and WGS net forward reaction rate (b), for 300 mA cm^{-2}. At 15 atm, methane is produced at the free-stream side of the anode, and consumed at the electrolyte. There is a relatively insignificant amount of WGS reaction from 0.0 to 1 mm as shown in the inset of b.

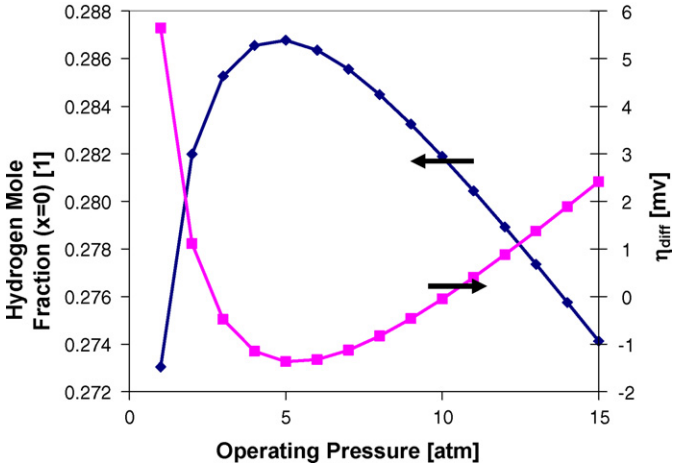

Fig. 8. Hydrogen mole fraction at the anode–electrolyte interface, and concentration overpotential loss due to gas phase diffusion (300 mA cm^{-2}).

at higher pressures via the reverse MSR reaction. This can also be seen in Fig. 6b, which shows the methane profile through the electrode. The concentration of methane first decreases as pressures increase to about 7–8 atm. At pressures greater than 8 atm, methane concentrations go up.

Fig. 7a shows the net rate of methane reformation through the electrode. As pressure increases, methane near the free-stream side of the anode is first consumed in the MSR reaction up until pressures greater than 7 atm. At pressures 8 atm and higher, methane is produced. This rate behavior is consistent with the hydrogen profiles shown in Fig. 6a. Fig. 7b shows the net forward WGS reaction rate (observe the change in scale on the x-axis). At the very outer electrode surface there is an increase in reaction rate with pressure. However, at depths within the anode, the WGS reaction rate may first increase with pressure, but then gradually decrease with pressure due to the near full consumption of any non-equilibrium CO at the outer domain. The pressure dependency shown here is taken to arise from the combined effect of MSR reaction which produces CO at pressures less than 8 atm, and diffusion.

Fig. 8 shows the effect of operating pressure on mole fraction of hydrogen at the electrolyte side of the electrode, and the voltage loss (overpotential) due to gas diffusion losses which is calculated by the traditional overpotential relation

$$\eta_{\text{diff}} = -\frac{RT}{2F}\ln\left(\frac{\left(\frac{P_{H_2}}{P_{H_2O}}\right)_{FS}}{\left(\frac{P_{H_2}}{P_{H_2O}}\right)_{E}}\right) \tag{31}$$

where the subscript FS denotes data taken at the free-stream, and the subscript E denotes data taken at the electrolyte. For simple pure diffusion problems, Eq. (31) shows the voltage loss

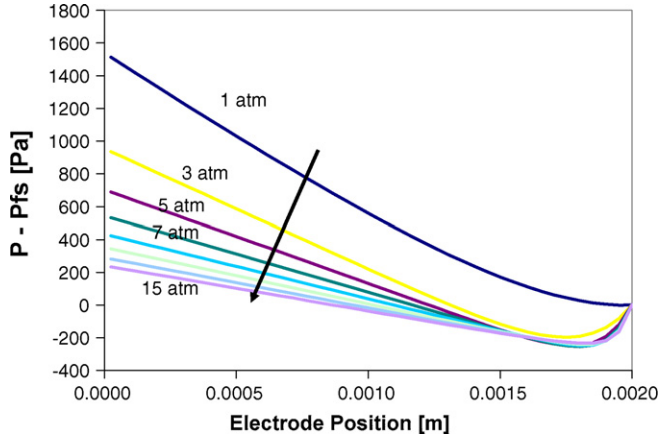

Fig. 9. Total pressure distribution through the electrode relative to the free-stream (P_{fs}) (300 mA cm^{-2}).

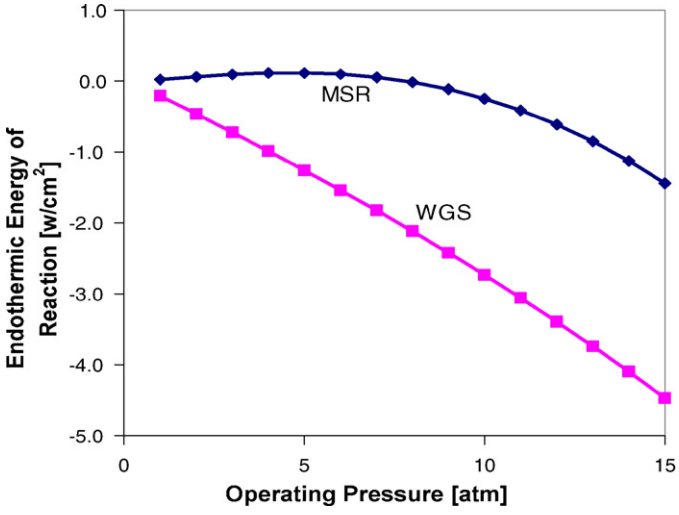

Fig. 10. Anode electrode inlet edge cooling (+) and heating (−) as a function of operating pressure for 300 mA cm^{-2}.

that results from the concentration loss resulting from gas phase diffusion through the electrode. (Positive values indicate a voltage loss.) As shown in Fig. 8, as pressure increases from 1 to 5 atm, the hydrogen concentration has a small but quick rise in value and the diffusion overpotential quickly decreases. At pressures above about 3 atm, the overpotential goes negative (i.e., there is no voltage loss due to changes in the H_2/H_2O concentration ratio through the electrode.) This behavior results from the competition between diffusion transport losses which reduce the H_2/H_2O ratio and the production of hydrogen from the MSR reaction. It is evident that while consumption of hydrogen and production of steam would lower the H_2/H_2O ratio at the electrolyte, sufficient hydrogen is being produced and transported within the electrode to overcome this reduction. At pressures above 10 atm, the overpotential becomes positive as the amount of hydrogen falls at the electrolyte interface.

Fig. 9 shows the total pressure in the anode relative to the free-stream operating pressure. Recall that in prior work it sometimes assumed that the pressure through the electrode is constant, and thereby allowing the use of Graham's law, Eq. (30). As can be seen from these results, the pressure departs most significantly from the free-stream value for the 1 atm pressure condition. However, even for very high operating pressures, the use of Graham's law will be invalid given the known specie fluxes (e.g., $n_{H_2} = -n_{H_2O}$). It is fundamentally impossible for pressure to be constant within anode electrodes in general. It has even been shown from calculations at current loads of 0.0 A cm^{-2} that a total pressure differential ($\sim$−400 Pa) exists between the electrolyte and the free stream for this particular inlet edge of the anode. This arises due to the balance of the hydrogen mole flux out of the anode electrode (generated by reforming and water-gas shift), and the flux of carbon monoxide and methane into the anode.

Fig. 10 shows the magnitude of heating and cooling vs. operating pressure for the 300 mA cm^{-2} load. Again, the MSR reaction, when operated in the forward direction, will cool the cell, whereas the WGS reaction, when operated in the forward direction, will heat the cell. As shown in Fig. 10, for pressures less than about 7 atm, the MSR offers some mild amount of cooling. Because of the strong WGS reaction, however, there is an overall net heating of the cell over the entire pressure domain studied. The level of heating is relatively low for ambient pressure operation. However, fairly strong heating occurs at pressures greater than 4 atm. It is important to understand, however, that the conditions modeled are most applicable to the inlet edge of the anode. It is at this edge that the supplied reactants will first hit the anode material and react. Given the rates of reaction seen above, the supplied anode reactants will quickly equilibrate. That is, the gas will converted to near equilibrium conditions over a small distance into the cell. Past this distance, no more heating due to non-equilibrium chemistry will occur, and the only heating will be due to the electrochemical conversion of fuel. Finally, it is also important to understand that other thermal transport mechanisms are present that also need to be taken into account (e.g., radiation and convective transport) in order to solve the full thermal state of the cell. These results, however, highlight that a significant portion of heating may also come from the fuel reactants supplied by the gasifier.

5. Summary and conclusion

In this paper the effect of operating at higher pressure and on coal syngas was investigated via detailed modeling. For representative syngas conditions, the following key features of the cell operation were determined:

- There is a maximum pressure of about 8 atm at which hydrogen is produced via the methane steam reforming reaction; operating at higher pressures results in methane production.
- The water-gas shift reaction rate increases up to about 7 atm; operating at higher pressures reduced the shift of CO to H_2.
- The overpotential due to diffusion losses, as described by changes in hydrogen at the electrolyte interface, shows a decrease in value as pressure increases up to about 5 atm after which diffusion loss again increases.
- Because of chemical non-equilibrium in the syngas mixture, the inlet edge to the anode is faced with significant heating, primarily due to the net forward water-gas shift reaction.

It is concluded here that research opportunities exist to experimentally identify the level of heating that might occur on the anode, and its mechanical effect on the anode. That is, will such level of heating at the inlet cause severe temperature gradients on existing SOFC technology that has been designed for other fuel types and operating pressures, or is the conductivity of the materials and other thermal transport mechanisms sufficient to dissipate this heat sufficiently to avoid mechanical and structural problems?

References

[1] "FutureGen: Integrated Hydrogen, Electric Power Production and Carbon Sequestration Research Initiative", United States Department of Energy Office of Fossil Energy Report to Congress, March, 2004.
[2] T. Kivisaari, P. Bjornbom, C. Sylwan, B. Jacquinot, D. Jansen, A. de Groot, The feasibility of a coal gasifier combined with a high temperature fuel cell, Chem. Eng. J. 100 (2004) 167–180.
[3] M.C. Williams, J.P. Strakey, W.A. Surdoval, The U.S. Department of Energy, Office of Fossil Energy Stationary Fuel Cell Program, J. Power Sources 143 (2005) 191–196.
[4] C. Higman, M. van der Burgt, Gasification, Elsevier, 2003, pp. 85–127.
[5] J. Ratafia-Brown, L. Manfredo, J. Hoffmann, M. Ramezan, Major environment aspects of gasification-based power generation technologies: final report, U.S. Department of Energy, 2002, pp. 39–59.
[6] S.C. Stultz, J.B. Kitto (Eds.), Steam, 40th ed., Babcock and Wilcox, 1992, pp. 17.1–17.17.
[7] S. Shaffer, Gasified coal success for Delphi SOFC, Fuel Cells Bulletin, November, 2003, p. 2.
[8] O. Solcova, H. Snajdaufova, V. Hejtmanek, P. Schneider, Textural properties of porous solids in relation to gas transport, Chem. Papers 53 (6) (1999) 396–402.
[9] Y. Matsuzaki, M. Hishinuma, I. Yasuda, Electrochemical characteristics of a Ni/YSZ cermet electrode on YSZ in a H_2–H_2O–CO–CO_2 system, Electrochem. Soc. Proc. 99-19 (1999) 560–567.
[10] Y. Matsuzaki, I. Yasuda, Electrochemical oxidation of H_2 and CO in a H_2–H_2O–CO–CO_2 system at the interface of a Ni/YSZ Cermet electrode and YSZ electrolyte, J. Electrochem. Soc. 147 (5) (2000) 1630–1635.

[11] A.L. Dicks, Advances in catalysts for internal reforming in high temperature fuel cells, J. Power Sources 71 (1998) 111–122.
[12] R. Peters, R. Dahl, U. Kluttgen, C. Palm, D. Stolten, Internal reforming of methane in solid oxide fuel cell systems, J. Power Sources 106 (2002) 238–244.
[13] P. Aguiar, C.S. Adjiman, N.P. Brandon, Anode-Supported intermediate temperature direct internal reforming solid oxide fuel cell. I. Model-based steady-state performance, J. Power Sources 138 (2004) 120–136.
[14] E. Achenbach, E. Riensche, Methane/steam reforming kinetics for solid oxide fuel cells, J. Power Sources 52 (1994) 283–288.
[15] T. Ackmann, L.G.J. de Haart, D. Stolten, Modeling of mass transport in planar substrate type SOFCs, in: J. Huijsmans (Ed.), Proceedings of the Fifth European Solid Oxide Fuel Cell Forum, Lucerne, Switzerland, 1–5 July, 2002.
[16] S. Bebelis, A. Zeritis, C. Tiropani, S.G. Neophytides, Intrinsic kinetics of the internal steam reforming of CH_4 over Ni/YSZ-cermet catalyst-electrode, Ind. Eng. Chem. Res. 39 (2000) 4920–4927.
[17] W. Lehnert, J. Meusinger, F. Thom, Modeling of gas transport phenomena in SOFC anodes, J. Power Sources 87 (2000) 57–63.
[18] W. Drescher, J. Lehnert, Meusinger, Structural properties of SOFC anodes and reactivity, Electrochem. Acta 43 (1998) 3059–3068.
[19] B.A. Haberman, J.B. Young, Three-dimensional simulation of chemical reacting gas flows in the porous support structure of an integrated-planar solid oxide fuel cell, Int. J. Heat Mass Trans. 47 (2004) 3617–3629.
[20] E.S. Hecht, G.K. Gupta, H. Zhu, A.M. Dean, R.J. Kee, L. Maier, O. Deutschmann, Methane reforming kinetics within a Ni/YSZ SOFC anode support," Appl. Catal. A: Gen., in press.
[21] E.A. Mason, A.P. Malinauskas, Gas Transport in Porous Media: The Dusty Gas Model, Chemical Engineering Monographs, vol. 17, Elsevier, New York, 1983.
[22] E.L. Cussler, Diffusion. Mass transfer in fluid systems, 2nd ed., Cambridge University Press, 1997.
[23] L.W. Warren, Verification and application of the dusty gas model, Ph.D. Thesis, University Microfilms Inc., Ann Arbor, MI, 1969.
[24] J. Divisek, D. Froning, W. Lehnert, J. Meusinger, U. Stimming, Transport processes and methane reforming reactions in the SOFC-cermet anodes, in: IEA, 10th SOFC Workshop, vol. 1, Les Diableret, Switzerland, 1997.
[25] S.V. Patankar, in: W.J. Winkowycz, E.M. Sparrow (Eds.), Numerical Heat Transfer and Fluid Flow, Series in Computational Methods in Mechanics and Thermal Sciences, McGraw-Hill Book Company, New York, 1980.
[26] R.R. Remick, C.J. Geankoplis, Ternary diffusion of gases in capillaries in the transition region between Knudsen and molecular diffusion, Chem. Eng. Sci. 29 (1974) 1447–1455.
[27] H. Yakabe, M. Hishinuma, M. Uratani, Y. Matsuzaki, I. Yasuda, Evaluation and modeling of performance of anode-supported solid oxide fuel cell, J. Power Sources 86 (2000) 423–431.
[28] R. Suwanwarangkul, E. Croiset, M.W. Fowler, P.L. Douglas, E. Entchev, M.A. Douglas, Performance comparison of Fick's, dusty-gas and Stefan–Maxwell models to predict the concentration overpotential of a SOFC anode, J. Power Sources 122 (2003) 9–18.
[29] R.E. Williford, L.A. Chick, G.D. Maupin, S.P. Simner, Diffusion limitations in the porous anodes of SOFCs, J. Electrochem. Soc. 150 (8) (2003) A1067–A1072.
[30] Y. Yi, A.D. Rao, J. Brouwer, G.S. Samuelson, Fuel flexibility study of an integrated 25 kW SOFC reformer System, J. Power Sources 144 (2005) 67–76.
[31] E.J. Hoffman, Coal Gasifiers, The Energon Company, P.O. Box 1352, Laramie, Wyoming, 1981, p. 82070.
[32] S.H. Clarke, A.L. Dicks, K. Pointon, T.A. Smith, A. Swann, Catalytic aspects of the steam reforming of hydrocarbons in internal reforming fuel cells, Catal. Today 38 (1997) 411–423.
[33] A. Weber, B. Sauer, A.C. Muller, D. Herbstritt, E. Ivers-Tiffee, Oxidation of H_2, CO and methane in SOFC's with Ni/YSZ-cermet anodes, Solid State Ionics 152-153 (2002) 543–550.
[34] A. Gunji, C. Wen, J. Otomo, T. Kobayashi, K. Ukai, Y. Mizutani, H. Takahashi, Carbon deposition behavior on Ni–ScSZ anodes for internal reforming solid oxide fuel cells, J. Power Sources 131 (2004) 285–288.
[35] W. Kasta, C.R. Hohenthanner, Mass transfer within the gas-phase of porous media, Int. J. Heat Mass Transfer 43 (2000) 807–823.